Wind tunnel testing of an avian-inspired morphing wing with distributed pressure sensing

Mario Martinez Groves-Raines[1], Sergio A. Araujo-Estrada[2],
Abdulghani Mohamed[3], Simon Watkins[4] and Shane P. Windsor[5]

Abstract— Small fixed wing uncrewed air vehicles (UAVs) are often required to fly at low speeds and high angles of attack, particularly when operating in urban environments. This study focuses on the potential of combining two bio-inspired flight technologies to improve maneuverability under these conditions. The outstanding flight agility of birds is believed to be enabled by the capability to sense the airflow over their wings and morph their wing surfaces accordingly. To test the benefits of combining these abilities a wind tunnel model able to perform an avian-inspired wing sweep motion incorporating two arrays of pressure sensors was developed. Aerodynamic load results highlight strong changes to the pitching moment produced by the change in wing sweep angle. This suggests that wing sweep can be an alternative or complementary mechanism for pitch attitude control, improving control authority at high angles of attack. On the other hand, pressure sensing data shows the ability of these sensors to detect the fine details of the onset of aerodynamic stall. The combination of these two novel technologies is suggested as a potential method to improve UAV pitch control when flying at low speeds, when the aircraft is most susceptible to environmental disturbances.

Index Terms— bio-inspired; morphing; distributed pressure sensing; wing sweep; pitch control

I. INTRODUCTION

Uncrewed Air Vehicles (UAVs) are used for a growing number of applications such as delivery of goods, rescue, surveillance, etc. Fixed-wing UAVs have advantages in terms of range, endurance and speed with respect to multi-copter drones/UAVs. However, operation at low altitudes in complex environments, such as urban air-spaces, requires high levels of maneuverability and the ability to deal with wind gusts and high-levels of turbulence [1], which can cause issues for fixed-wing UAVs [2]–[4].

Birds are capable of flying in complex environments such as woodlands and cities, and display ability to adapt to unpredictable flow environments [5]. This ability is thought to be partly enabled by bird's complex wing surfaces, capable of changing shape during flight in order to optimize their performance for certain flight conditions. These changes in wing shape are known as wing morphing, and their effects on aerodynamic forces and moments are poorly understood. Birds rely on many degrees-of-freedom (DOFs) through which they can change the shape of their wings [6], [7]. Bird wing morphing during gliding flight is of particular interest due to the similarities it shares with fixed-wing UAV flight, in terms of size and flight environment. Wing sweep, also referred to as the flexion and extension of the wing, has been highlighted as one of the main morphing DOF changing the overall shape of a bird's wing during gliding flight [8], [9].

Furthermore, evidence suggests that distributed flow sensing plays an important role enabling bird flight agility [10]. Conventional aircraft and UAVs rely on a range of attitude sensors that measure the velocities and accelerations affecting the center of mass which feed into the aircraft's control system. These types of inertial sensors work well when assuming rigid aircraft and linear aerodynamics, but have limitations when used for flexible aircraft flying in highly unsteady conditions [11]. Wing flexibility and flight in turbulent conditions are both challenges for small fixed-wing UAVs. Thus, the use of distributed pressure sensors on UAVs may allow real-time characterization of the state of the flow around UAV wings to potentially optimize performance and aid in gust mitigation [12].

Avian wing morphing has been the source of inspiration of a number of fixed-wing UAVs [13]. A few of these have focused on the development of avian-inspired morphing structures mimicking wing sweep in birds, with the goal of improving the maneuverability of fixed-wing UAVs. Some designs can exclusively change sweep, such as Greatwood *et al* [14] where the wing of the UAV rotated about the wing root for perching maneuvers. Some designs are more relatable to avian-inspired wing sweep and are commonly composed of discrete feather elements that can overlap during sweep. Di Luca *et al* [15] and Hui *et al* [16] separately proposed similar designs mimicking wrist sweep bird morphing. Both studies highlighted the effectiveness of this type of bio-inspired wing sweep for changing aerodynamic forces and optimizing flight performance. Ajanic *et al* [17] developed a flying UAV with avian-inspired morphing wings and tail that showed how the combined morphing of the two lifting surfaces could be optimized for particular mission demands: more maneuverable or more stable aircraft. Chang *et al* [8] proposed a more unconventional design by developing a robotic hybrid wing using real pigeon feathers

[1]Mario Martinez Groves-Raines, Department of Aerospace Engineering, University of Bristol, Bristol, United Kingdom
`mario.grovesraines.2016@bristol.ac.uk`

[2]Sergio A. Araujo-Estrada, Department of Aerospace Engineering, University of Bristol, Bristol, United Kingdom
`s.araujoestrada@bristol.ac.uk`

[3]Abdulghani Mohamed, Department of Aerospace Engineering and Aviation, RMIT University, Melbourne, Australia
`abdulghani.mohamed@rmit.edu.au`

[4]Simon Watkins, Department of Aerospace Engineering and Aviation, RMIT University, Melbourne, Australia
`simon.watkins@rmit.edu.au`

[5]Shane P. Windsor, Department of Aerospace Engineering, University of Bristol, Bristol, United Kingdom
`shane.windsor@bristol.ac.uk`

to form the morphing surface, and showed that wing sweep is effective for roll control.

In comparison to UAVs, biological fliers have evolved various ways of sensing other flight-relevant information beyond inertial and visual. For instance, insects have campaniform sensilla and hair-like structures distributed throughout their wings and bodies to sense the loads acting on their wings as well as the state of the flow around them [18]–[20]. Research suggest that mechanoreceptors in the wings of birds [21] may enable flow sensing [22], while muscle spindles provide information on the wing loading state [23]. Similar to birds, bats have muscle spindles [24] and hair-like structures that are sensitive to flow changes [25].

Longitudinal static stability refers to the tendency of an aircraft to return to equilibrium when disturbed (normally in pitch), which directly affects its controllability and stability. A strongly longitudinally stable aircraft will be able to mitigate effects of turbulence by producing higher restoring moments [26], beneficial in cruise flight. However, aircraft that are very stable also tend to be less maneuverable in flight. Fixed-wing UAVs are likely to encounter missions where they need to transition from fast speed cruise to agile maneuvering around complex environments. Wing sweep morphing wings can potentially allow this change in longitudinal static stability by shifting the aerodynamic center, hence optimizing the aircraft's shape for a particular stage of a mission. Previous designs and studies into wing sweep morphing have focused on its potential for roll control authority and lateral stability [8], [15], [16], with little attention drawn to the pitch stability and control potential of symmetric sweep actuation.

The potential of both wing-morphing and distributed sensing to improve the maneuverability of UAVs has been demonstrated separately. Wing sweep morphing has previously been shown to improve maneuverability of small sized UAVs [14], [15], [17]. Moreover, it has been noted that during complex maneuvers using wing morphing, such as perching landing or tight turns, it is likely that some sections of the wing may reach aerodynamic stall [14]. UAVs flying at low Reynolds numbers are more susceptible to local stall as a product of atmospheric turbulence [27]. Morphing aircraft could therefore benefit from having accurate sensors that could detect the onset of stall to avoid compromising flight safety. Previous research into the potentials of distributed pressure sensors shows how these can be used to detect aerodynamic phenomena like flow separation [11], [28] and improve attitude control of MAVs [29]. However, the fusion of wing morphing and distributed pressure sensing has not yet been explored.

This work aims to investigate the potential benefits of combining bio-inspired wing-morphing with distributed pressure sensing to improve the maneuverability of UAVs operating in urban scenarios.

The rest of this paper is organized as follows: Section II describes the experimental platforms and methodology used in this work, as well as their main characteristics. Section III presents wind tunnel characterization results of a bio-inspired morphing wing instrumented with an array of distributed pressure sensors. Section IV summarizes the information presented in this paper, and discusses identified limitations and potential avenues for future work. Lastly, Section V concludes this paper with some general remarks.

II. METHODS

A. Wing model

A bio-inspired sweep morphing wing was designed and built in order to carry out wind-tunnel experiments assessing the effects of this novel degree-of-freedom. The morphing was inspired by the wrist sweep (also referred to as flexion/extension motion) commonly observed in gliding and soaring birds. The wing was also equipped with two arrays of pressure taps located on the inboard (fixed) and outboard (morphing) sections of the wing. The wind-tunnel model (half-model) wingspan for an extended wing configuration was 0.626 m, and the inboard section had a span of 0.3 m with a NACA 0012 airfoil section. The chord of the inboard section was 0.2 m, and was constructed using an internal plywood structure of ribs and spars, with a main aluminium spar and a rear carbon fiber spar. The airfoil shape was achieved using shrink wrap film. The morphing or outboard section was composed by thin artificial feather-like elements that overlapped over each other during morphing, as shown in Figure 1a. These were fabricated using 1.5 mm thick laser-cut acrylic sheet. All elements were linked together at a common joint or pivot. The feather elements were labeled 1 to 5 from the leading edge to the trailing edge. The shape and length of each element varied depending on their position. Different materials were trialed for the manufacture of the morphing joint, but the high loads required the joint to be made of aluminium. Weight of the model was not optimised for free-flight tests.

Two separate pressure tap sections were fitted to the model. The inboard section consisted on a chord-wise array of 19 pressure taps placed at 0.263 m from the wing root, close to junction of the fixed and morphing wing sections. A 3-D-printed insert was manufactured to house the inboard pressure taps (shown in Figure 2b). The pressure port locations were labeled as follows: LE as leading edge, T01 to T09 for the top surface sensors from leading to trailing edge, and B01 to B09 for the bottom surface locations from leading to trailing edge. The four pressure sensors on the morphing section of the wing were also embedded into a 3-D-printed insert, which was attached to the leading edge of the feather element 1, and ran span-wise when the wing was extended. These were labeled as MT01 and MT10 for the morphing-top-surface sensors from inboard to outboard of the span, and MB01 and MB10 for the morphing-bottom-surface sensors from inboard to outboard. Locations of both sensor arrays are shown in Figures 1a and 2a.

The morphing of the wing was achieved through a high voltage servo (MacGregor MG7232HV 31.5 kg cm/0.09 s), mounted on the inboard section of the wing. The movement was translated from the servo to feather element 1 through a servo arm, which allowed the leading edge of the outboard
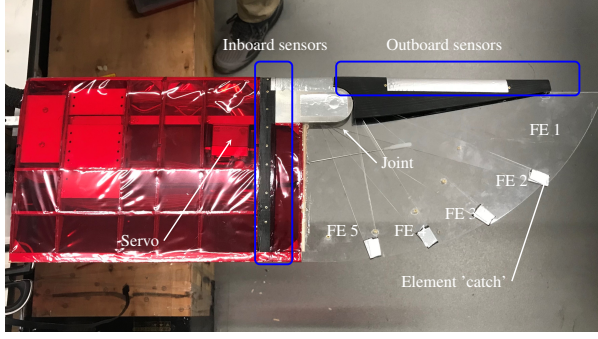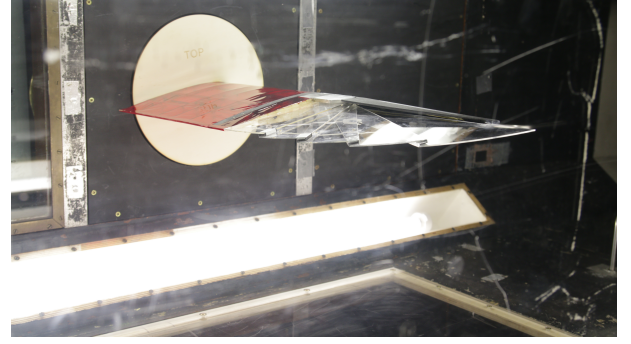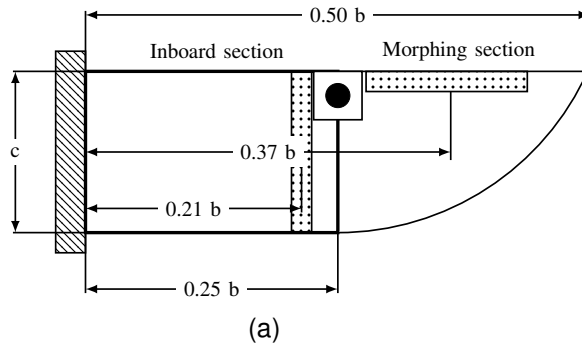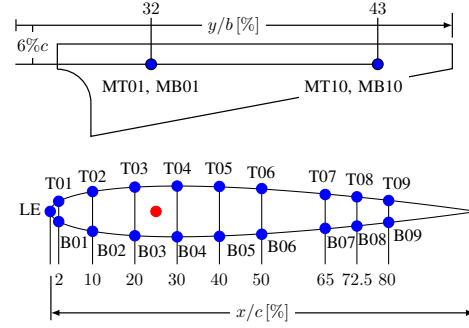
Fig. 1. Wing model experimental platform: (a) model component parts and (b) model installed in wind tunnel.

Fig. 2. Wing model experimental platform schematic diagram: (a) model's main dimensions and (b) pressure array distribution.

section to sweep by a total of $40°$ with respect to the fully extended configuration. Table I shows how wing area (S), semi-span ($b/2$) and mean aerodynamic chord (c) are affected by the change of servo command angle (δ_{cmd}) and actual wing sweep angle (δ_w), characterized to ensure repeatability for the five desired wing sweep positions. Note that this relationship was not linear since the motion from the rotational servo was not in the same plane as the wing sweep rotation. In order to achieve an even distribution of the feather elements, and to avoid different spreading of the feathers through different tests, elastic rubber bands were used to link together all the individual feather elements. Based on previously reported research [11], two different pressure sensors were used in the sensing array: one with a $\pm500\,\text{Pa}$ measurement range (SDP36, Sensirion) and another with a $\pm2\,\text{kPa}$ measurement range (MPXV7002, Freescale Semiconductor) for conditions where saturation was expected for the lower range sensors.

B. Testing apparatus

The bio-inspired morphing wing was tested in the University of Bristol low turbulence wind tunnel. The wind tunnel has a turbulence intensity of less than $0.1\,\%$ [30]. The working section has a rectangular cross-section of $0.8\,\text{m} \times 0.6\,\text{m}$ with corner fillets, and a length of $1.6\,\text{m}$. A rough depiction of the experimental setup is given in Figure 3.
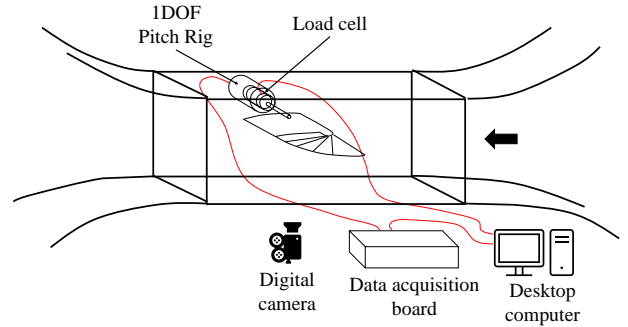

Fig. 3. Wind tunnel setup and equipment.

A one-degree-of-freedom pitch rig was attached to the side of the wind tunnel, holding the bio-inspired morphing wing. This rig allowed for accurate adjustments of the pitch

TABLE I

WING MODEL CHARACTERISTICS

δ_{cmd} (°)	-55	-13	11	32	51
δ_w (°)	40	30	20	10	0
S (m²)	0.0973	0.0993	0.1023	0.1057	0.1087
$b/2$ (m)	0.570	0.597	0.613	0.625	0.626
c (m)	0.1707	0.1663	0.1668	0.1691	0.1736

angle of the wind tunnel model, as well as the potential for dynamic actuation of the wing in pitch. The rig was used in previous experiments performed in the low turbulence wind tunnel, and has shown to be both effective and accurate [11], [28]. Details on the data acquisition system characteristics have been previously reported [11]. The DOF is driven by a servo motor (Schneider Electric model LXM32MD30M2, Rueil- Malmaison, France), and the aerodynamic loads were captured using a small load cell (ATI Industrial Automation model Mini 45, Apex, North Carolina) placed between the model and the pitch rig.

C. Data calibration, correction and normalization

Experiments were carried out to calibrate the various instruments and sensors used in this work. For brevity, details on this calibration process are given in the Appendix.

The calibrated force and moment data was normalized to capture the effect of wing sweep on the forces and moments per unit area, using the effective area for each wing sweep angle. This normalization method has been previously used [9], although alternative methods have been reported where the loads are normalized by a reference area (either at extended or retracted pose) [15], [17]. The aerodynamic loads were normalized as follows:

$$C_D = \frac{D}{\frac{1}{2}\rho V^2 S} \qquad C_L = \frac{L}{\frac{1}{2}\rho V^2 S} \qquad C_M = \frac{M}{\frac{1}{2}\rho V^2 S c} \tag{1}$$

where D, L and M refer to drag, lift and pitching moment respectively, ρ is air density ($1.225\,\mathrm{kg/m^3}$), V is the nominal wind speed, S is the effective wing area at a particular wing sweep angle, and c is the mean geometric chord taken along the whole semi-span for a particular wing sweep angle. Results for absolute and normalized aerodynamic forces and moments are presented and discussed in Section III-A, highlighting the differences between normalized and absolute force measurements.

The calibrated pressure readings were normalized using:

$$C_{P_i} = \frac{P_i - P_\infty}{\frac{1}{2}\rho V^2} \tag{2}$$

with P_i the pressure measured by sensor for sensor i (with $i \in \{\mathrm{LE, T1, ..., T9, B1, ..., B9, MT1, MB1, MT10, MB10}\}$), P_∞ the static pressure in the free-stream and C_{P_i} the pressure coefficient for sensor i. For location of pressure sensors see Figure 2b.

In the next section, we present results from characterization experiments using the equipment and methods described here.

III. Results

Using the wind tunnel model described in Section II-A, experiments were carried out in order to characterize the aerodynamic loads and pressure readings through a wide range of conditions. The test conditions were altered independently, setting airspeed at $V \in \{8, 10, 12, 14, 16, 18, 20\}\mathrm{m/s}$, model pitch angle or angle of attack to $\alpha \in \{0, 5, 10, 15, 20\}°$ and wing wrist sweep angle at five different settings $\delta_w \in$

$\{0, 10, 20, 30, 40\}°$. In terms of wing sweep values, $\delta_w = 0°$ refers to a fully extended wing, whereas $\delta_w = 40°$ refers to a fully retracted or swept-back wing. Two separate sets of tests were performed to produce the results presented below. Static tests, which refer to those measurements taken for a fixed airspeed, angle of attack and wing sweep angle, gathered load cell and pressure signal data for a time window of approximately $15\,\mathrm{s}$. The other set of tests was referred to as quasi-static, and these consisted on angle of attack sweeps at very low rates ($q = 1°/\mathrm{s}$), where no dynamic effects are expected to be seen [11]. These results were used to show the onset of stall with more accuracy than static tests as well as helping to reduce the uncertainty between angle-of-attack static test data-points. Load cell data for the experimental tests was collected at $60\,\mathrm{Hz}$, whereas pressure sensor data was collected at $200\,\mathrm{Hz}$.

A. Aerodynamic loads characteristics

Figure 4 displays the main aerodynamic forces and moments of interest against angle of attack at the different sweep angle poses tested during the static experiments. Results here are presented for wind speeds of $V = 20\,\mathrm{m/s}$, corresponding to a Reynolds number of approximately $230\,000$. Quasi-static test results for the two extreme poses are also shown in Figure 4. Firstly, Figure 4a shows how the absolute lift force produced by the model increased over the whole range of positive angles of attack for fully extended wing configurations ($\delta_w = 40°$). This tendency is accentuated for angles of attack prior to the stall region. Simultaneously, in Figure 4b the overall absolute aerodynamic drag of the wing also increases with the degree of extension. Figure 4c reflects how absolute pitching moment seems to be the most sensitive parameter to the change in wing wrist sweep δ_w. By tucking the wing backwards at the wrist location, there is a large increase in the negative slope of the pitching moment versus angle of attack curve, which will directly affect the static stability of the wing. Pitching moment results presented here show the isolated aerodynamic effects of wing sweep, without accounting for the inertial effects produced by the shift of the center of mass. Details on the normalization of pitching moment are provided in the Appendix. Comparing the proportional effect of wing sweep on the three absolute aerodynamic parameters shown in Figures 4a, 4b and 4c, indicates that the parameter most sensitive to changes in wing sweep is pitching moment. The quasi-static data shows that aerodynamic stall or airflow detachment begins at $\alpha_{stall} \approx 12.0°$ for this particular airspeed. No significant difference is seen between the onset of stall of an extended wing configuration with respect to a tucked wing configuration. After aerodynamic stall occurs, pitching moment curve slope drastically increases for all wing sweep configurations, indicating a clear tendency for restoring/nose-down pitching moments.

Figures 4d-f display normalized aerodynamic coefficients that also correspond to the tests performed at $V = 20\,\mathrm{m/s}$. Figure 4e shows the drag coefficient for both the static and quasi-static cases selected as before. The drag coef-
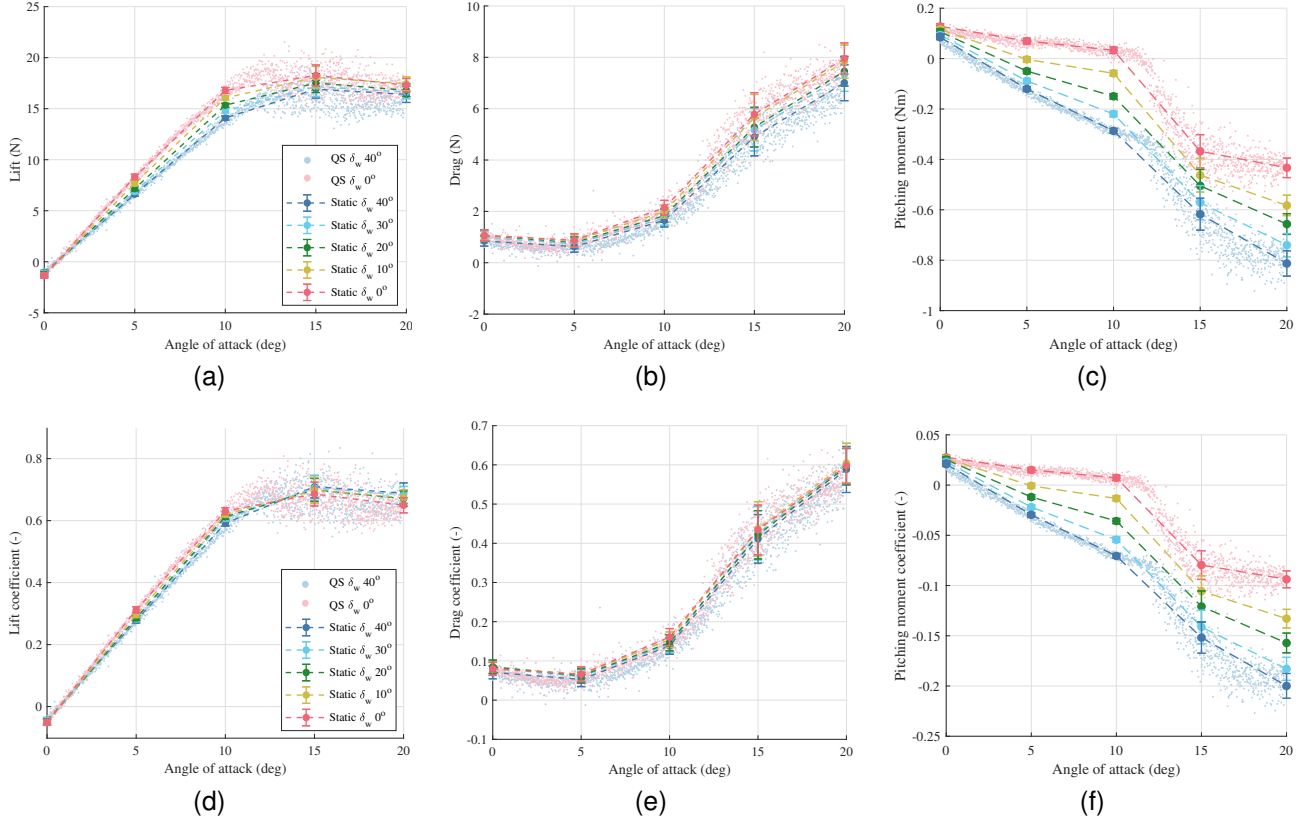
Fig. 4. Aerodynamic measurements from the wing load cell against angle of attack for $V = 20\,\mathrm{m/s}$, showing absolute (a) lift, (b) drag and (c) pitching moment and normalized parameters (d) lift coefficient, (e) drag coefficient and (f) pitching moment coefficient; overlaying static and quasi-static test results, showing the agreements between tests.
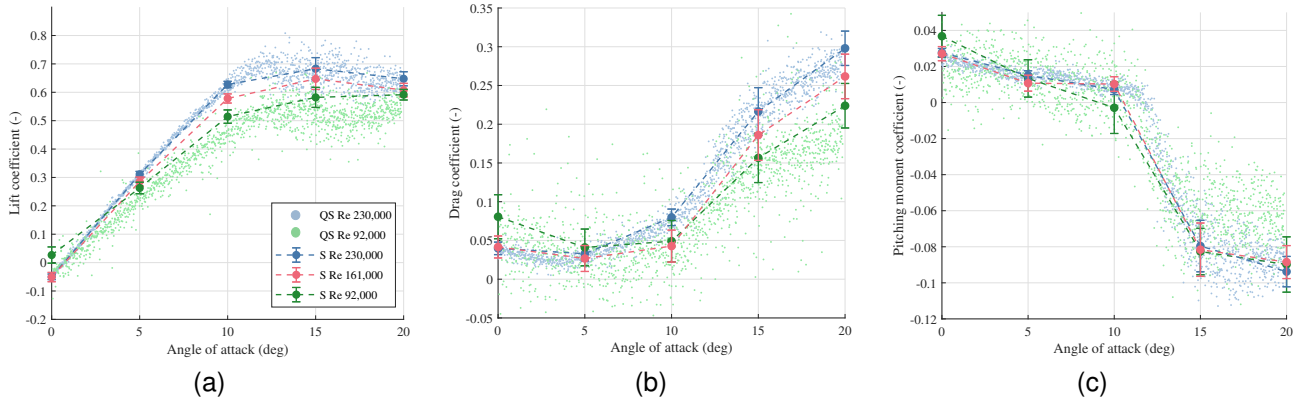

Fig. 5. Aerodynamic load coefficients against angle of attack for the fully extended configuration, showing how these are affected for different Reynolds numbers tested.

ficient curves show a typical quadratic shape for α values before stall, with a minimum drag coefficient value of approximately $C_{D_{min}} = 0.03$ when $\alpha_{C_{D_{min}}} = 5.0°$ for the static case. Quasi-static results show a slightly lower drag coefficient at roughly $\alpha_{C_{D_{min}}} = 3.0°$. Figure 4d shows the aerodynamic lift coefficient C_L. When plotted against α, curves show a linear trend before aerodynamic stall is reached. Lift coefficient curves are similar for all morphing configurations likely due to the nature of the normalization: retracted wings generate less lift but also have lower

wing areas than those of extended wings. For a reference $\alpha = 0.0°$, the model was producing a slight negative lift coefficient of -0.06, likely due to the complex geometry of the outboard wing section. The average curve slope for $V = 20\,\mathrm{m/s}$ was $C_{L_\alpha} = 3.9$ for $0.0° < \alpha <= 9.5°$ and the maximum lift coefficient $C_{L_{max}} = 0.76$, which was achieved at $\alpha_{C_{L_{max}}} \approx 11.8°$. Furthermore, Figure 4d shows a slight benefit on lift coefficient for extended wing configurations before the stall point at $\alpha_{stall} \approx 12.0°$. For post-stall α angles, lift coefficient is maximized with fully tucked wing

configurations, i.e. $\delta_w = 40°$. Finally, Figure 4f shows the pitching moment coefficient C_M calculated through the agreed normalization. C_M for all wing sweep configurations changed linearly with α for incidence values before stall. As for absolute results in Figure 4c, wing sweep configuration has a strong effect on pitching moment at high angles of attack, even after the corresponding normalization. This is not the case for lift and drag force curves after normalization.

Results also show that wing sweep angle has little or no effect on pitching moment at low angles of attack, whereas the effects are maximized for high angles of attack prior to stall. Bigger sweep deflections (swept back wings) increased the negative pitching moment curve slope. The slope of the curve relating C_M and α (C_{M_α}) has strong links to the longitudinal static stability of the aircraft, with more negative slopes resulting in more stable aircraft. However, C_{M_α} here is entirely dependent on the location of the pivot point (location along the chord where we are measuring pitching moments), which is roughly located at the 1/4 chord of the inboard section of the wing. The aerodynamic center closely matches the pivot point for the fully extended configuration, as the slope of the curve is $C_{M_\alpha} \approx 0$. As the wing sweeps back, the aerodynamic center moves away from the pivot, generating more negative values of C_{M_α}. All wing sweep configurations produced C_M curves with negative slopes, which meant all wings were stable in pitch. For the case when $\alpha = 10°$, C_M was approximately 5 times greater when adopting a fully tucked configuration $\delta_w = 40°$ as opposed to the extended case when $\delta_w = 0°$. This highlights the potential of wing wrist sweep δ_w to be used for pitch attitude and stability control.

Figure 5 shows the effect of Reynolds number. Results presented are for the fully extended wing case ($\delta_w = 0°$) only, showing overlaid quasi-static and static test results. Reynolds number effects are as expected for lift and drag coefficients in Figures 5a and 5b, increasing the slope of their curves as Reynolds numbers increase. On the other hand, Figure 5c shows that Reynolds number does not seem to have a large effect on the pitching moment coefficient across the angles of attack tested. Similar curves were seen for other wing configurations tested.

B. Pressure signal characteristics

Figure 6 shows the characteristic response of selected pressure sensors in coefficient form against α for $V = 20\,\mathrm{m/s}$ from quasi-static tests. There was good agreement between the quasi-static and static data, but the static data has been omitted for ease of interpretation. For the pressure coefficient definition and the sensor location the reader is referred to Section II. Panels (a) to (c) have been arranged to show pressure measurements moving progressively along the wing span, with: Figure 6a showing sensors T3 and B3 on the inboard chord-wise array, Figure 6b showing sensors MT1 and MB1 on the inboard end of the wing's morphing-section and Figure 6c showing sensors MT10 and MB10 on the outboard end of the wing's morphing-section. Each panel also shows the sensors signals for $\delta_w = 0°$ and $\delta_w = 40°$,

i.e., extended and retracted configurations, respectively. It can be observed that the pressure signals encode a wealth of data. For instance, before the stall region, the signals for sensors located on the top surface (i.e., T3, MT1, MT10) all increased with α. Around the stall onset region, the characteristics became highly nonlinear. Note that the sensor location was related to the α point where this nonlinear behavior began. For $\delta_w = 0°$, this happened at $\alpha \approx 10°$ for sensor MT10, whereas for MT1 this was at $\alpha \approx 11°$ and for T1 it was at $\alpha \approx 12°$. A similar trend was observed for $\delta_w = 40°$, with α values of approx. $8°$, $9°$ and $12°$ for MT10, MT1 and T1, respectively. Similar behavior was observed for sensors located on the bottom surface (i.e., B3, MB1, MB10), albeit with an opposing sign. These results are in agreement with the aerodynamic load ones presented in Figures 4 and 5 and suggest that an early wing-stall warning system could be implemented by tracking the local α corresponding to the onset of the nonlinear behavior.

It was found that this characteristic was easier to observe when the signals from sensors on the same chord-wise location but on opposing surfaces were subtracted. Figure 7 shows the result when the signals from B1, MB1 and MB10 were subtracted from those corresponding to T1, MT1 and MT10, respectively. Panels (a) to (f) show the signals plotted against α for values of $\delta_w = 0$, 20 and $40°$ (increasing left to right) and values of $V = 8$ and $20\,\mathrm{m/s}$ (increasing top to bottom). In general, it was observed that T3-B3 (in red) displayed very similar behavior for all δ_w and V conditions, with strong correlation to stall at $\alpha \approx 12°$. MT1-MB1 (in blue) showed strong correlation with stall in the region $10° \leq \alpha \leq 11°$ and the signal-to-noise-ratio increasing with V. While MT10-MB10 (in green) showed weak correlation with stall for $V \leq 10\,\mathrm{m/s}$. However, for $V \geq 12\,\mathrm{m/s}$, there was a strong correlation with stall.

Overall these results highlight the potential of using the signals from the distributed pressure sensing array to implement an early wing-stall warning system. In the following section, we discuss how distributed sensing could be used in combination with wing morphing to improve the maneuverability of a UAV flying in an urban scenario at high-α and low-V values.

IV. Discussion

Avian wing morphing could be an inspiration route for the improvement of UAV flight control. These experiments explored the potential benefits of avian morphing as an alternative control surface. Pitch control in conventional aircraft and fixed-wing UAVs is achieved through the deflection of a tail elevator. As implemented in this study, wing sweep produces considerable changes in pitching moment, particularly at high angles of attack. However, the changes to pitching moment produced by wing sweep δ_w are not as large as those produced by conventional tail elevators, being roughly one order of magnitude lower than typical conventional small UAV configurations [31], [32]. Thus, wing sweep may not be suitable for fully replacing conventional tail elevators. However, combining wing sweep and tail elevator for pitch
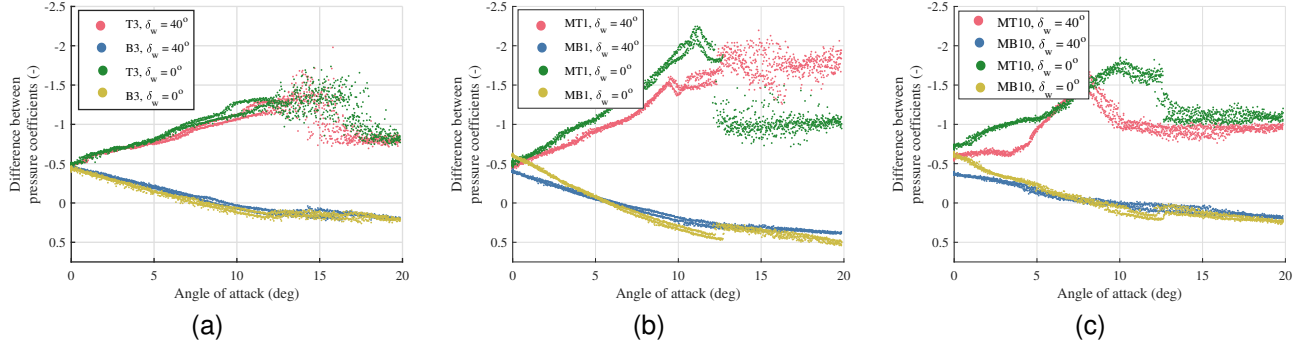
Fig. 6. Selected pressure coefficients against α for $V = 20\,\text{m/s}$: (a) fixed-wing section T3, (b) morphing-wing section MT1 and (c) morphing-wing section MT10. Please refer to Figure 2b for sensor location.

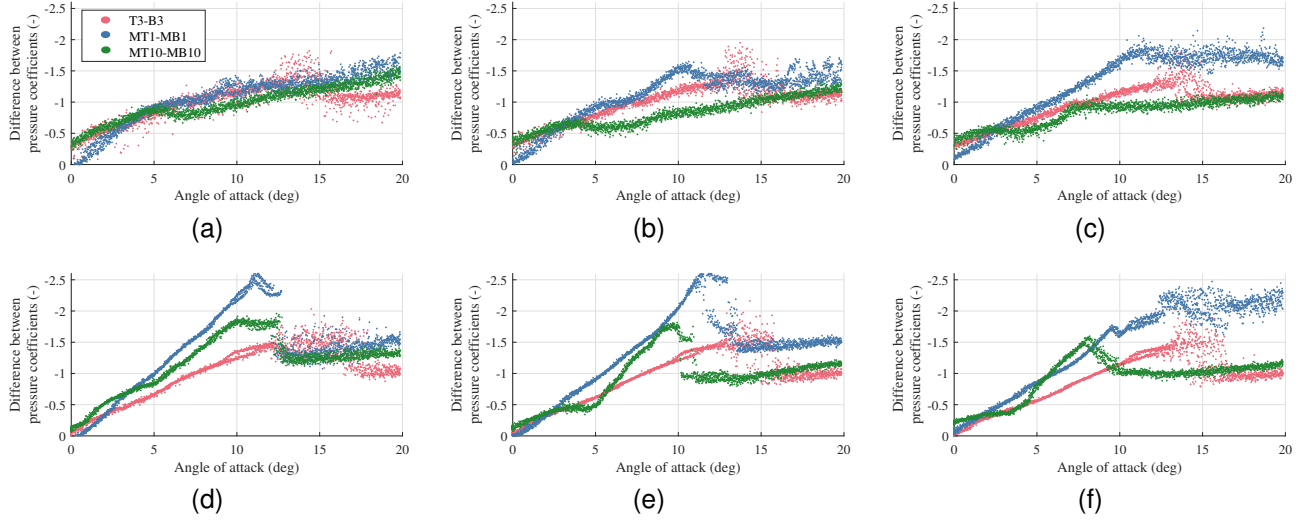Fig. 7. Characteristic Reynolds number and wing-wrist deflection effect against α when selected pressure signals are subtracted: (a) $V = 8\,\text{m/s}$ and $\delta_w = 0°$, (b) $V = 8\,\text{m/s}$ and $\delta_w = 20°$, (c) $V = 8\,\text{m/s}$ and $\delta_w = 40°$, (d) $V = 20\,\text{m/s}$ and $\delta_w = 0°$, (e) $V = 20\,\text{m/s}$ and $\delta_w = 20°$, and (f) $V = 20\,\text{m/s}$ and $\delta_w = 40°$,.

control could improve the performance of fixed-wing UAVs in different ways. Mathematically this can be expressed as follows

$$C_M = C_{M_0} + C_{M_\alpha}\alpha + C_{M_q}\frac{c}{2V_a}q + C_{M_{\delta_e}}\delta_e + C_{M_{\delta_w}}\delta_w \quad (3)$$

with C_{M_0} the pitching moment coefficient at $\alpha = 0°$, C_{M_α} the contribution of angle of attack to pitching moment, $C_{M_q}\frac{c}{2V_a}q$ the damping term, $C_{M_{\delta_e}}$ the influence of tail elevator angle δ_e to pitching moment and $C_{M_{\delta_w}}$ the contribution of wing sweep. The addition of the $C_{M_{\delta_w}}$ term would allow for a lower reliance on tail elevator angle δ_e, which would increase the aircraft's control authority in pitch.

Having both an elevator and wing sweep could allow trade-offs to be made between the degree of pitch control authority and the area or lever arm of the horizontal tail plane. This could bring benefits in terms of aerodynamic efficiency, maneuverability, and/or weight.

It is likely that birds with short tails make use of wing sweep for pitch control [33]. In essence, shorter tails would reduce the stability contribution of the tail and amplify the effect of wing sweep, with sweep having a larger effect on the shift of the overall position of the aerodynamic center. This would suggest more stable poses for tucked wings and more maneuverable poses with extended wings. Further analysis is be required to assess the effects and trade-offs of combining wing sweep and tail-planes for pitch stability and control.

When flying at low speeds aircraft have to adopt higher angles of incidence to generate the required lift. At high angles of attack control effectiveness of the wing sweep degree of freedom is enhanced as observed in the data in Table II. This behavior is not seen for conventional tail elevators of fixed-wing UAVs, for example a Bixler 2 UAV showed a relatively constant value of C_{M_δ} between $0°$ and $5°$ incidence [31]. Hence, aircraft could benefit from having a sweep wing DOF for flight at low speeds and high angles of attack, increasing control authority in pitch. Wing sweep would however be particularly inefficient at controlling pitch at low angles of attack close to $0°$, as presented in Table II. The concept of wing sweeping for pitch control can only work when the wing is generating lift, as opposed to a

conventional tail and elevator. This highlights the benefits of using conventional elevators for pitch control at low angles of attack. The main benefit of wing sweep for pitch control therefore would appear to be at high angles of attack, where conventional trailing edge surfaces are limited by their stall deflection angle.

TABLE II
WING WRIST SWEEP PITCHING MOMENT CONTROL
DERIVATIVE COEFFICIENTS

Coefficient	AoA	Reynolds number		
		92000	161000	230000
$C_{M_{\delta_w}}$	0°	-0.0248	-0.0151	-0.0098
$C_{M_{\delta_w}}$	5°	-0.05371	-0.05506	-0.0631
$C_{M_{\delta_w}}$	10°	-0.08769	-0.108	-0.1127

The results presented in Section III-A also suggest that wrist sweep morphing is an effective way of adjusting the longitudinal static stability in a bio-inspired UAV wing. Longitudinal static stability is a characteristic that reflects a trade-off between flight maneuverability and robustness to perturbations. Small UAVs may benefit from transitioning between these two states, depending on the characteristics of the environment in which they are flying. We suggest that wing sweep may be used as a an effective way of modifying longitudinal static stability in flight.

Wing sweep deflection was shown to affect aerodynamic lift at high angles of attack prior to stall (Figure 4a). This suggests that wing sweep could be used to adjust lift production without the need for changing the pitch attitude of the aircraft. This would bring advantages in terms of stabilizing sensors, for example vision based sensors, commonly used in small UAVs.

The use of this type of wing morphing, relying on overlapping discrete feather elements, would challenge the implementation of conventional ailerons used for roll control. However, the asymmetric sweep of area-changing morphing wings like these has been shown to be an effective way of controlling roll attitude [8], [15], [17]. Further analysis is needed to explore the effects of wing sweep on roll control and how this may couple with the proposed pitch control function.

The pressure signals characterization results showed that there is a wealth of information on the state of the flow encoded in them. These results agree with previously reported work looking at aerodynamic state estimation in wind tunnel experiments with array of sensors mounted on wings [34]–[39], as well as work looking at pressure sensing-based angle of attack estimation for flight control [40], and pressure and strain sensing-based estimation of aerodynamic loads and state [11].

The main benefit of having sweep morphing wings for pitch attitude control has been highlighted as its potential to improve flight at low speeds and high angles of attack. These flight conditions are very challenging in terms of controllability. They require flying at angles of attack close to aerodynamic stall, which is likely to change due to

atmospheric turbulence and the presence of gusts [27]. The potential of pressure sensors to detect the onset of stall could be a good solution to avoid unfavorable flight conditions. A pre-stall warning signal could be used to trigger a change in wing sweep or tail elevator to avoid flow separation. The non-linear nature of turbulent flows is likely to have asymmetric effects on the wings. Sensors on both wings could command asymmetric adjustments of wing sweep to counteract for these non-linearities.

Future work could look further into characterizing the aerodynamic loads and flow state through experiments where the sweep morphing degree-of-freedom is dynamically actuated to study the aerodynamic force and control response for different ranges of motion and different actuation frequencies.

Moreover, previous authors have used similar sweeping wings for roll control. Further work is needed to explore the combined use of this mechanism for both roll and pitch control, as well as the couplings between them.

As implemented here the wrist sweep wing was not optimized for flight. Further work needs to be conducted considering the model proportions (i.e., dimensions of wing's fixed and morphing part) and mass, along with optimizing the placement of pressure sensors. This will allow an assessment to be made as to the advantages of the sweep wing DOF against the added mass and flight control complexity it entails.

Another potential research avenue would be to combine these two bio-inspired concepts with Machine Learning approaches to produce nonlinear estimators and fully exploit the information contained in the distributed pressure sensing array signals.

Lastly, closed loop control experiments could be carried out to verify experimentally the ideas from the case study presented here.

V. CONCLUSIONS

A novel approach to the improvement of fixed-wing UAV maneuverability has been presented. The benefits of combining wing morphing and distributed pressure sensing, two biology-inspired technologies, are explored through the analysis of load and pressure measurements.

The avian-inspired wing was characterized in the wind tunnel for a range of speeds and poses. A wing sweep was shown to be an effective way of changing pitching moment, which suggests that wing sweep could be used as an effective mechanism to control the aircraft's pitch attitude. Moreover, the effect of wing sweep angle δ_w on C_{M_α} confirmed the initial hypothesis that wing sweep is directly linked to the longitudinal static stability of the aircraft. Thus, wing sweep may be used to transition from more robust or stable poses into more maneuverable or agile configurations.

The signals from the distributed pressure sensing array showed good agreement with the aerodynamic state and loads. More importantly, a high correlation with the onset of stall along the wingspan was observed. This suggests that distributed pressure sensing could be used to implement an

early warning wing-stall system by tracking the state of the flow around the wing and highlight the advantages of this approach over point-based measurements.

By combining these two bio-inspired concepts, future UAV designs could improve their maneuverability and robustness while operating in complex urban scenarios and through highly-nonlinear flow conditions.

REFERENCES

[1] A. Mohamed, K. Massey, S. Watkins, and R. Clothier, "The attitude control of fixed-wing MAVS in turbulent environments," *Progress in Aerospace Sciences*, vol. 66, pp. 37–48, 2014.

[2] S. Watkins and G. Vino, "The turbulent wind environment of birds, insects and MAVs," *15th Australasian Fluid Mechanics Conference*, no. December, pp. 1–4, 2004.

[3] S. Watkins, A. Mohamed, A. Fisher, R. Clothier, R. Carrese, and D. F. Fletcher, "Towards autonomous MAV soaring in cities: CFD simulation, EFD measurement and flight trials," *International Journal of Micro Air Vehicles*, vol. 7, no. 4, pp. 441–448, 2015.

[4] A. Mohamed, S. Watkins, R. Clothier, and M. Abdulrahim, "Influence of Turbulence on MAV Roll Perturbations," *International Journal of Micro Air Vehicles*, vol. 6, no. 3, pp. 175–190, 2014.

[5] G. K. Taylor, A. C. Carruthers, T. Y. Hubel, and S. M. Walker, "Wing morphing in insects, birds and bats: Mechanism and function," in *Morphing Aerospace Vehicles and Structures*. John Wiley Sons, Ltd, 2012, pp. 11–40.

[6] D. D. Chin, L. Y. Matloff, A. K. Stowers, E. R. Tucci, and D. Lentink, "Inspiration for wing design: How forelimb specialization enables active flight in modern vertebrates," *Journal of the Royal Society Interface*, vol. 14, no. 131, 2017.

[7] B. Baliga, I. Szabo, and D. L. Altshuler, "Range of motion in the avian wing is strongly associated with flight behavior and body mass," *Science Advances*, vol. 5, no. 10, 2019.

[8] E. Chang, L. Y. Matloff, A. K. Stowers, and D. Lentink, "Soft biohybrid morphing wings with feathers underactuated by wrist and finger motion," *Science Robotics*, vol. 5, no. 38, 2020.

[9] B. K. Van Oorschot, E. A. Mistick, and B. W. Tobalske, "Aerodynamic consequences of wing morphing during emulated take-off and gliding in birds," *Journal of Experimental Biology*, vol. 219, no. 19, pp. 3146–3154, 2016.

[10] R. E. Brown and M. R. Fedde, "Airflow Sensors in the Avian Wing," *Journal of Experimental Biology*, vol. 179, no. 1, pp. 13–30, 1993.

[11] S. A. Araujo-Estrada and S. P. Windsor, "Aerodynamic State and Loads Estimation Using Bioinspired Distributed Sensing," *Journal of Aircraft*, pp. 1–13, 2020.

[12] A. Mohamed, S. Watkins, R. Clothier, M. Abdulrahim, K. Massey, and R. Sabatini, "Fixed-wing MAV attitude stability in atmospheric turbulence - Part 2: Investigating biologically-inspired sensors," *Progress in Aerospace Sciences*, vol. 71, pp. 1–13, 2014.

[13] D. Li, S. Zhao, A. Da Ronch, J. Xiang, J. Drofelnik, Y. Li, L. Zhang, Y. Wu, M. Kintscher, H. P. Monner, A. Rudenko, S. Guo, W. Yin, J. Kirn, S. Storm, and R. D. Breuker, "A review of modelling and analysis of morphing wings," *Progress in Aerospace Sciences*, vol. 100, no. May, pp. 46–62, 2018.

[14] C. Greatwood, A. Waldock, and T. Richardson, "Perched landing manoeuvres with a variable sweep wing UAV," *Aerospace Science and Technology*, vol. 71, pp. 510–520, 2017.

[15] M. Di Luca, S. Mintchev, G. Heitz, F. Noca, and D. Floreano, "Bioinspired morphing wings for extended flight envelope and roll control of small drones," *Royal Society Publishing*, vol. 7, no. 1, 2017.

[16] Z. Hui, Y. Zhang, and G. Chen, "Aerodynamic performance investigation on a morphing unmanned aerial vehicle with bio-inspired discrete wing structures," *Aerospace Science and Technology*, vol. 95, p. 105419, 2019.

[17] E. Ajanic, M. Feroskhan, S. Mintchev, F. Noca, and D. Floreano, "Bioinspired wing and tail morphing extends drone flight capabilities," *Science Robotics*, vol. 5, no. 47, 2020.

[18] M. H. Dickinson, "Comparison of Encoding Properties of Campaniform Sensilla on the Fly Wing," *Journal of Experimental Biology*, vol. 151, no. 1, pp. 245–261, 1990.

[19] K. H. Taylor, G. and S. Simpson, "Sensory systems and flight stability: What do insects measure and why?" in *ADVANCES IN INSECT PHYSIOLOGY: INSECT MECHANICS AND CONTROL*. John Wiley Sons, Ltd, 2016, pp. 231–316.

[20] H. Ai, A. Yoshida, and F. Yokohari, "Vibration receptive sensilla on the wing margins of the silkworm moth Bombyx mori," *Journal of Insect Physiology*, vol. 56, no. 3, pp. 236–246, 2010.

[21] W. Hörster, "Histological and electrophysiological investigations on the vibration-sensitive receptors (herbst corpuscles) in the wing of the pigeon (columba livia)," *Journal of Comparative Physiology A*, vol. 166, no. 5, pp. 663–673, 1990.

[22] R. E. Brown and M. R. Fedde, "Airflow sensors in the avian wing," *Journal of Experimental Biology*, vol. 179, pp. 13–30, 1993.

[23] D. L. Altshuler, J. W. Bahlman, R. Dakin, A. H. Gaede, B. Goller, D. Lentink, P. S. Segre, and D. A. Skandalis, "The biophysics of bird flight: functional relationships integrate aerodynamics, morphology, kinematics, muscles, and sensors," *Canadian Journal of Zoology*, vol. 93, no. 12, pp. 961–975, 2015.

[24] A. Hedenström and L. Christoffer Johansson, "Bat flight: aerodynamics, kinematics and flight morphology," *Journal of Experimental Biology*, vol. 218, no. 5, pp. 653–663, 2015.

[25] S. Sterbing-D'Angelo, M. Chadha, C. Chiu, B. Falk, W. Xian, J. Barcelo, J. M. Zook, and C. F. Moss, "Bat wing sensors support flight control," *Proceedings of the National Academy of Sciences of the United States of America*, vol. 108, no. 27, pp. 11 291–11 296, 2011.

[26] F. Irving, "Chapter 3 - conditions for static stability," in *An Introduction to the Longitudinal Static Stability of Low-Speed Aircraft*, F. Irving, Ed. Pergamon, 1966, pp. 26–34.

[27] S. Watkins, S. Ravi, and B. Loxton, "The effect of turbulence on the aerodynamics of low Reynolds number wings," *Engineering Letters*, vol. 18, no. 3, 2010.

[28] S. A. Araujo-Estrada and S. P. Windsor, "Artificial Neural Network-Based Flight Control Using Distributed Sensors on Fixed-Wing Unmanned Aerial Vehicles," in *AIAA Scitech 2020 Forum*. Reston, Virginia: American Institute of Aeronautics and Astronautics, 1 2020.

[29] A. Mohamed, M. Marino, S. Watkins, and R. Clothier, "Bioinspired Wing-Surface Pressure Sensing for Attitude Control of Micro Air Vehicles," *Journal of Aircraft*, vol. 3, no. 52, pp. 827–838, 2015.

[30] R. Barret, "Design and performance of a new low turbulence wind tunnel at Bristol University," *The Aeronautical Journal (1968)*, vol. 88, no. 873, pp. 86–90, 1984.

[31] A. Waldock, C. Greatwood, F. Salama, and T. Richardson, "Learning to Perform a Perched Landing on the Ground Using Deep Reinforcement Learning," *Journal of Intelligent and Robotic Systems: Theory and Applications*, vol. 92, no. 3-4, pp. 685–704, 2018.

[32] A. Guerra-Langan, S. Araujo Estrada, and S. Windsor, "Reinforcement Learning to Control Lift Coefficient Using Distributed Sensors on a Wind Tunnel Model," in *AIAA SCITECH 2022 Forum*, 2022.

[33] A. L. Thomas and G. K. Taylor, "Animal flight dynamics I. Stability in gliding flight," *Journal of Theoretical Biology*, vol. 212, no. 3, pp. 399–424, 2001.

[34] S. Callegari, M. Zagnoni, A. Golfarelli, M. Tartagni, A. Talamelli, P. Proli, and A. Rossetti, "Experiments on an aircraft flight parameter detection by on-skin sensors," *Sensors and Actuators A: Physical*, vol. 130-131, pp. 155–165, 2006.

[35] H. Fei, R. Zhu, Z. Zhou, and J. Wang, "Aircraft flight parameter detection based on a neural network using multiple hot-film flow speed sensors," *Smart Materials and Structures*, vol. 16, no. 4, p. 1239, 2007.

[36] I. Samy, I. Postlethwaite, D.-W. Gu, and J. Green, "Neural-network-based flush air data sensing system demonstrated on a mini air vehicle," *Journal of Aircraft*, vol. 47, no. 1, pp. 18–31, 2010.

[37] R. Que and R. Zhu, "Aircraft aerodynamic parameter detection using micro hot-film flow sensor array and BP neural network identification," *Sensors (Switzerland)*, vol. 12, no. 8, 2012.

[38] K. T. Magar, G. W. Reich, C. Kondash, K. Slinker, A. M. Pankonien, J. W. Baur, and B. Smyers, "Aerodynamic parameters from distributed heterogeneous cnt hair sensors with a feedforward neural network," *Bioinspiration & Biomimetics*, vol. 11, no. 6, p. 066006, 2016.

[39] R. J. Laurence, B. M. Argrow, and E. W. Frew, "Wind tunnel results for a distributed flush airdata system," *Journal of Atmospheric and Oceanic Technology*, vol. 34, no. 7, pp. 1519–1528, 2017.

[40] K. T. Wood, S. Araujo-Estrada, T. Richardson, and S. Windsor, "Distributed pressure sensing–based flight control for small fixed-wing unmanned aerial systems," *Journal of Aircraft*, vol. 56, no. 5, pp. 1951–1960, 2019.

APPENDIX

A brief description of the models obtained from calibration experiments is presented next with the corresponding parameter values given in Table III. First, experiments were conducted to obtain the mapping between the deflection of the servo actuating the artificial feathers and the resulting wing wrist deflection, as well as the effect of this deflection on the wing's area, semi-span and equivalent mean geometric chord. These were performed using a digital camera, a protractor and the wing model. The process is described next. First, the maximum (fully tucked) and minimum (fully extended) servo commands were identified and, using the digital camera image as reference, the protractor was aligned with the wing's morphing-section leading edge. This was defined as $\delta_w = 0°$. Then the servo deflection was slowly changed until the next target wing wrist deflection was reached, recording the resulting servo deflection command. The process was repeated until the maximum wing wrist deflection was reached. The identified wing model's morphing characteristics are given in Table I.

TABLE III

MATHEMATICAL MODEL PARAMETERS

Parameter (Units)	Value	95% bounds	R^2
$\mu_{\delta_{cmd}}$ (°)	−2.0		
δ_{cmd_R} (°)	106.0		
δ_{w_R} (°)	40.0		0.9997
a_{δ_w}	0.2246	(0.2135, 0.2357)	
b_{δ_w}	0.215	(0.1619, 0.2681)	
a_b (m)	0.626		0.9934
b_b	0.4205	(0.4031, 0.4379)	
a_S (m^2)	-0.02915	(-0.031, -0.0273)	0.9934
c_S (m^2)	0.1087		
$a_{\ell_{CG}}$ (cm)	8.391	(8.33, 8.453)	
$b_{\ell_{CG}}$	0.7528	(0.7464, 0.7591)	0.9185
m_{MW} (kg)	0.1668		
m_T (kg)	1.8254		
m_b (kg)	0.4625		
θ_{LC} (°)	13.0		0.9071
a_{M_Z} (N m)	-0.08748	(-0.08811, -0.08685)	
b_{M_Z} (N m)	-0.8552		

Using data from Table I, a mathematical model describing δ_w as a function of δ_{cmd} was obtained as

$$\hat{\delta}_{cmd} = \frac{\delta_{cmd} + \mu_{\delta_{cmd}}}{\delta_{cmd_R}} + 0.5$$

$$\delta_w = \delta_{w_R} \cos\left(2\pi a_{\delta_w}(\hat{\delta}_{cmd}) + b_{\delta_w}\right) \tag{4}$$

with $\hat{\delta}_{cmd}$ the normalized servo command input, $\mu_{\delta_{cmd}}$ the center-value servo command input, δ_{cmd_R} the servo command range, δ_{w_R} the wing wrist deflection range, and scaling parameters a_{δ_w} and b_{δ_w}.

In a similar fashion, models were obtained for both b and S as a function of δ_w

$$b = a_b \cos\left(b_b \frac{\delta_w}{\delta_{w_R}}\right) \tag{5}$$

$$S = a_S \sin\left(b_b \frac{\delta_w}{\delta_{w_R}}\right) + c_S \tag{6}$$

with a_b, b_b and a_S scaling parameters corresponding to b and S, respectively, and b_S a bias term.

Inertial effects were observed in the pitching moment channel. These were produced by the displacement of the center of gravity (CG) when the wing is swept. To ensure that pitching moment results reflected only aerodynamic effects a correction was applied following the model below

$$\Delta\ell_{CG}(\delta_w) = a_{\ell_{CG}} \sin\left(b_{\ell_{CG}} \frac{\delta_w}{\delta_{w_R}}\right) \tag{7}$$

$$\Delta M = m_{MW} g \Delta\ell_{CG} \tag{8}$$

with $\Delta\ell_{CG}$ the CG displacement in m, $a_{\ell_{CG}}$ the measured CG displacement range in m, $b_{\ell_{CG}}$ a scaling factor, m_{MW} the mass of the mobile morphing wing components in kg and g the acceleration due to Earth's gravitational pull (9.81 m/s^2).

The load cell output signals (F_X, F_Y and M_Z) were calibrated by measuring the forces exerted by 4 known-masses at various pitch angles and using the resulting data to fit a mathematical model matching each of the known-mass forces. This model was also used to remove the inertial effects from the load measurements and is given by

$$F_X = m_T g \sin(\alpha + \theta_{LC}) - m_b g \cos(\theta_{LC}) \tag{9}$$

$$F_Y = m_T g \cos(\alpha + \theta_{LC}) + m_b g \sin(\theta_{LC}) \tag{10}$$

$$M_Z = a_{M_Z} \alpha + b_{M_Z} \tag{11}$$

with m_T the sum of the masses of the rig and morphing wing model, θ_{LC} the load cell installation angle, m_b the pre-loading mass, a_{M_Z} the change in moment in the M_Z channel with α and b_{M_Z} a bias term.

Then, the corrected loads (without inertial effects) were computed as

$$F_{X_C} = F_{X_M} - F_X \tag{12}$$

$$F_{Y_C} = F_{Y_M} - F_Y \tag{13}$$

$$M_{Z_C} = M_{Z_M} - (M_Z + \Delta M) \tag{14}$$

$$\tag{15}$$

with F_{X_M} and F_{Y_M} the forces measured by the load cell for the X and Y channels, M_{Z_M} the moment measured by the load cell for the Z channel, F_{X_C} and F_{Y_C} the corrected loads for the X and Y channels, and M_{Z_C}, the corrected moment for the Z channel. Lastly, the loads expressed in wind axes were obtained using

$$D = F_{X_C} \cos(\alpha + \theta_{LC}) - F_{Y_C} \sin(\alpha + \theta_{LC}) \tag{16}$$

$$L = F_{X_C} \sin(\alpha + \theta_{LC}) + F_{Y_C} \cos(\alpha + \theta_{LC}) \tag{17}$$

$$M = M_{Z_C} \tag{18}$$

where D, L and M have already been defined.

The pressure sensing array signals were calibrated against a calibrated digital manometer (FC0510 Micromanometer, Furness Controls Limited, Sussex, UK). Using the calibrated digital manometer, measurements were taken at various nominal pressures and then repeated using the custom pressure sensors. A mathematical model was fitted to the calibration data to provide the best match (in the maximum likelihood sense) between the measurements of the calibrated digital manometer and the custom pressure sensors.